

Alma Mater Studiorum Università di Bologna
Archivio istituzionale della ricerca

Increasing risk of another Cape Town "day Zero" drought in the 21st century

This is the final peer-reviewed author's accepted manuscript (postprint) of the following publication:

Published Version:

Pascale S., Kapnick S.B., Delworth T.L., Cooke W.F. (2020). Increasing risk of another Cape Town "day Zero" drought in the 21st century. PROCEEDINGS OF THE NATIONAL ACADEMY OF SCIENCES OF THE UNITED STATES OF AMERICA, 117(47), 29495-29503 [10.1073/pnas.2009144117].

Availability:

This version is available at: <https://hdl.handle.net/11585/850253> since: 2022-01-31

Published:

DOI: <http://doi.org/10.1073/pnas.2009144117>

Terms of use:

Some rights reserved. The terms and conditions for the reuse of this version of the manuscript are specified in the publishing policy. For all terms of use and more information see the publisher's website.

This item was downloaded from IRIS Università di Bologna (<https://cris.unibo.it/>).
When citing, please refer to the published version.

(Article begins on next page)

Increasing risk of another Cape Town “Day Zero” drought in the twenty-first century

Salvatore Pascale^{a,b,c,1}, Sarah B. Kapnick^b, Thomas L. Delworth^b, and William F. Cooke^{b,d}

^aDepartment of Earth System Science, Stanford University, Stanford CA; ^bNOAA/Geophysical Fluid Dynamics Laboratory, Princeton NJ; ^cAtmospheric and Ocean Sciences Program, Princeton University, Princeton, NJ; ^dCooperative Programs for the Advancement of Earth System Science (CPAESS), University Corporation for Atmospheric Research (UCAR)

This manuscript was compiled on December 14, 2020

1 **Three consecutive dry winters (2015-2017) in southwestern South**
2 **Africa (SSA) resulted in the Cape Town “Day Zero” drought in early**
3 **2018. The contribution of anthropogenic global warming to this pro-**
4 **longed rainfall deficit has previously been evaluated through obser-**
5 **vations and climate models. However, model adequacy and insuffi-**
6 **cient horizontal resolution make it difficult to precisely quantify the**
7 **changing likelihood of extreme droughts given the small regional**
8 **scale. Here we use a new high-resolution large ensemble to estimate**
9 **the contribution of anthropogenic climate change to the probability**
10 **of occurrence of multi-year SSA rainfall deficits in past and future**
11 **decades. We find that anthropogenic climate change increased the**
12 **likelihood of the 2015-2017 rainfall deficit by a factor of five-to-six.**
13 **The probability of such an event will increase from 0.7% to 25% by**
14 **the year 2100 under an intermediate-emission scenario (SSP2-4.5)**
15 **and to 80% under a high-emission scenario (SSP5-8.5). These re-**
16 **sults highlight the strong sensitivity of the drought risk in SSA to**
17 **future anthropogenic emissions.**

Drought | climate change detection | climate extremes | event attribution
| large ensemble simulations

1 The Day Zero Cape Town drought was one of the worst
2 water crises ever experienced in a metropolitan area (1, 2).
3 Droughts are a regular occurrence in SSA, having occurred
4 during the late 1920s, early 1970s, and more recently during
5 2003-2004 (Fig. 1a,b). However, the extended winter (April-
6 September, AMJJAS) three-year rainfall deficit (Fig. 1a-b; SI
7 Appendix, Fig. S1) which drove the 2015-2017 Cape Town
8 drought (2-8) was exceptional over the last century (4, 9).
9 Storage in reservoirs supplying water to 3.7 million people in
10 the Cape Town metropolitan area dropped to about 20% of
11 capacity in May 2018. As a consequence, strict water usage
12 restrictions were implemented to delay water levels reaching
13 13.5%, the level at which much of the city’s municipal supply
14 would have been disconnected (7), a scenario referred to as
15 “Day Zero” by the municipal water authorities (7). Above
16 average winter rain over the rest of the 2018 austral winter
17 allowed Cape Town to avoid the Day Zero scenario.

18 While poor water management practices and infrastructure
19 deficiencies worsened the crisis (10, 11), the 2015-2017 rainfall
20 deficit was the main driver of the drought (5). To facilitate
21 the improvement of water management practices and the
22 infrastructure necessary to make the system more resilient,
23 it is critical to first determine how likely a meteorological
24 drought like the one in 2015-2017 might be in the coming
25 decades. Increased aridity is expected in most of southern
26 Africa (12-14) as a consequence of the Hadley Cell poleward
27 expansion (4, 15-18) and southward shift of the Southern
28 Hemisphere jet stream (19). Second, the risk of more extreme
29 droughts should be quantified to understand the potential for

emerging risks that could make a Day Zero event in Cape
Town unavoidable.

Previous work (5) has suggested that the Day Zero drought
may have been made 1.4-to-6.4 times more likely over the last
century due to +1 K of global warming, with the risk expected
to scale linearly with one additional degree of warming. Such
estimates make use of statistical models of the probability dis-
tribution’s tail (e.g., the Generalized Extreme Value) applied
to observations and previous-generation (i.e., as those partici-
pating to the Coupled Model Intercomparison Project Phase 3
(20) and 5 (21)) climate models. CMIP3 and CMIP5 models
have been shown to have a systematically biased position of
the Southern Hemisphere jet stream toward the equator due
to insufficient horizontal resolution (19). This produces a large
uncertainty in model projections of jet stream shifts (22, 23),
thus hindering realistic projections of Southern Hemisphere
climate change. Furthermore, for hydroclimatic variables, a
statistical extrapolation of the probability distribution’s tail
might have inherent limitations in providing precise estimates
of the event probability of future extreme events, although its
precision profits from the use of large ensembles (24, 25).

Large ensembles of comprehensive climate models provide
thousands of years of data that allow direct construction of the
underlying probability distribution of hydroclimatic extremes
without relying on a hypothesized statistical model of extremes
(25, 26). South African winter rains have high interannual and
decadal variability due to El Niño-Southern Oscillation (27),

Significance Statement

The Cape Town “Day Zero” drought was caused by an exceptional three-year rainfall deficit. Through the use of a higher resolution climate model, our analysis further constrains previous work showing that anthropogenic climate change made this event five-to-six times more likely relative to early 20th century. Furthermore, we provide a clear and well-supported mechanism for the increase in drought risk in SSA through a dedicated analysis of the circulation response, which highlights how – as in 2015-17 – a reduction in precipitation during the shoulder seasons is likely to be the cause of drought risk in SSA in the 21st century. Overall, this study greatly increases our confidence in the projections of a drying SSA.

S. P. conceived the study, performed the analysis and wrote the initial draft of the paper. T. L. D. and W. F. C. designed the ensemble, and W. F. C. performed the numerical simulations. All authors took part in the discussion of the results and contributed to the writing.

The authors declare no competing interests.

²To whom correspondence should be addressed. E-mail: spascale@stanford.edu or pascaledeep@gmail.com

57 the Southern Annular Mode (28) and interdecadal variability
58 (29). A multi-decade to multi-century record may be required
59 to detect the emergence of statistically significant trends in
60 regional precipitation extremes. A large ensemble is thus a
61 powerful method to isolate, at the decadal timescale, internal
62 natural variability (e.g., SI Appendix, Fig. S2) from the forced
63 signal (30–32).

64 The SPEAR large ensemble

65 To tackle this problem, we use a comprehensive suite of new
66 large ensemble simulations from the newly developed Seamless
67 System for Prediction and Earth System Research (SPEAR)
68 global climate model developed (33) at the Geophysical Fluid
69 Dynamics Laboratory (GFDL, see Methods). SPEAR is the
70 latest GFDL modeling system for seasonal to multidecadal
71 prediction and projection, and it shares underlying component
72 models with the CM4 (34) climate model, which participates to
73 the Coupled Model Intercomparison Project Phase 6 (CMIP6)
74 (35). In particular, we use the medium horizontal atmospheric
75 resolution (50 km) version of SPEAR, i.e., SPEAR_MED,
76 which has been designed to study regional climate and ex-
77 tremes. The SPEAR_MED simulations include a 3,000-year
78 preindustrial control simulation (CTRL), and three 30-member
79 ensembles that account for changing atmospheric compositions
80 arising from natural sources only (NATURAL), and natural
81 plus anthropogenic sources (HIST+SSP2-4.5, HIST+SSP5-8.5,
82 Methods for details). The relatively high horizontal resolution
83 of SPEAR_MED – which makes this large ensemble unique – is
84 key to better resolve the steep coastal SSA topography, which
85 leads to orographic enhancement of rainfall during frontal
86 days (4). SPEAR_MED is an excellent tool to investigate
87 SSA droughts because it has a realistic representation of the
88 SSA winter rainfall pattern (Fig. 1c-d) and seasonal cycle
89 (Fig. 1f), and it correctly reproduces the amplitude of the
90 interannual, multiannual and decadal natural variability of
91 the SSA winter rainfall (SI Appendix, Fig. S3).

92 Event attribution to anthropogenic climate change

93 As anthropogenic global warming weakens the basic stationar-
94 ity assumption which has historically been at the foundation of
95 water management (36), two key questions are: to what extent
96 did anthropogenic global warming make the Day Zero drought
97 more likely? And: how will the probability of occurrence of
98 another similar or worse meteorological drought change in the
99 coming decades? To address these questions, we first assess
100 if the probability distribution of anomalies of the three-year-
101 mean Winter Rainfall Index (WRI, see Methods) has already
102 significantly changed. We directly compare the time-evolving
103 probability distribution associated with successive twenty-year
104 time windows with that associated with only internal climate
105 variability obtained from a long control run at preindustrial
106 forcing (CTRL; see Methods for details). The two probability
107 distributions are statistically indistinguishable at the 99.9%
108 level per the Kolmogorov-Smirnov test, during the twenty-year
109 period 1980-2000 (Fig. 2a), but then start to significantly dif-
110 fer from 1990-2010 onward (Fig. 2b-d). Hereafter we refer to
111 the 2015-2017 WRI negative anomaly as “event_1517”. The
112 average of the event_1517 probabilities in the five decades
113 1921-1970 is approximately 0.7% (Fig. 2e). This is slightly
114 smaller than the value from the 3,000-year preindustrial con-
115 trol run and with the NATURAL experiment (1%) – which

profit from the much longer time span (SI Appendix, Fig. S4a)
– but nevertheless consistent within the 95% uncertainty in-
terval. The event probability is stationary up to 1980-2000,
after which it starts increasing (Fig. 2e). For 2015-2017 the
event probability – obtained by linear interpolation of the
2000-2020 and 2010-2030 values, is 3.7 % with a [2.5%,4.7%]
95% confidence interval. This implies a risk ratio – i.e., the
ratio of the probability of the event at at given time to its
probability in the early 20th century – of 5.5 times, with a
confidence interval of 4 to 8 (Fig. 2g). Thus, an extreme event
that had an average recurrence interval (37) of one hundred
years in the early 20th century reduces to 25-year recurrence
interval by present day. This is consistent with previous work
(5) in spite of the different event definition between the two
studies.

Drought risk projections

In the high-emission scenario SSP5-8.5 (intermediate-emission
scenario SSP2-4.5), the event_1517 probability – i.e., the
likelihood that rainfall is below the event_1517 threshold for
any random three year segment within the twenty-year window
– is projected to rise to 20% (13%) around 2045 (Fig 2f and SI
Appendix, Figs. S5 and S6) and to reach 80% (25%) by the
end of this century. For the SSP5-8.5 (SSP2-4.5) scenario, the
likelihood of an event_1517 would thus increase by a factor of
120 (40) relative to earlier in the twentieth-century (Fig. 2h).
This implies that the expected number of such droughts in 2081-
2100 will be approximately probability \times (20 years/3 years), i.e.,
5.3 (2.3) under SSP5-8.5 (SSP2-4.5). Extending the finding
of previous studies (5) beyond +2K of mean global surface
temperature increase, we find that, for each degree of warming,
the risk ratio grows at a slower rate after a fast, ongoing
acceleration (SI Appendix, Fig. S7). This implies a transition
to substantially drier and persistent wintertime conditions
over SSA.

Using the same methodology (see Methods), we can also
estimate the distribution and the probability of occurrence of
a four-year WRI anomaly at the same intensity of event_1517
(Fig. 2i-j). This has not occurred yet but, if it occurred, could
lead to an unavoidable Day Zero. In the absence of anthro-
pogenic forcing (i.e., CTRL and NATURAL), such an event
has a probability of occurrence of 0.4% (vs. approximately
1% for a three-year drought). Presently, the probability of
occurrence for it to happen has already substantially increased
relative to the early 20th century (2%), and it is projected
to be 15% (8%) by mid-century under SSP5-8.5 (SSP2-4.5).
By the end of the 21st century, a four-year WRI anomaly will
be almost as likely as three-year rainfall anomaly of intensity
comparable to the 2015-2017 event.

This suggests that the duration of meteorological droughts
will increase in SSA. We estimate the probability distribution
of the severe (i.e., ≤ -6 mm month⁻¹) winter (i.e., AMJJAS)
WRI anomalies as a function of duration and intensity under
the SSP2-4.5 (Fig. 3a-c) and SSP5-8.5 scenario (Fig. 3d-f).
Historically, the largest (in magnitude) negative WRI anom-
alies typically last 1 year. There is a non-negligible probability
of two-to-three-year persisting anomalies at about -10 mm
month⁻¹, while anomalies lasting longer than three years are
unlikely (Fig. 3). Anthropogenic climate change will make
meteorological winter droughts lasting three to ten years more
likely and more acute, especially under the SSP5-8.5 scenario

176 (Fig. 3d-f).

177 Large scale circulation shifts

178 The future increase in the probability of occurrence of intense
179 and prolonged rainfall deficits (Fig. 2f and Fig. 3) is suggestive
180 of a substantial climatic shift in the mean wintertime condi-
181 tions of SSA in the coming decades. In agreement with state-
182 of-the-art general circulation models (6, 38), SPEAR_MED
183 indicates a substantial AMJJAS WRI reduction during the
184 twenty-first century (SI Appendix, Fig. S8a), especially in
185 the shoulder seasons of April-May and August-October (SI
186 Appendix, Fig. S8b). In both scenarios, the amplitude of the
187 shift will be outside the range of what could occur from low-
188 frequency internal climate variability in the decade 2020-2030
189 (Fig. 4a-c), but the magnitude of the negative anomaly will
190 be substantially larger under a high-emission scenario.

191 The prolonged rainfall deficit experienced during winters
192 2015-2017 occurred along with positive large scale anomalies in
193 sea level pressure on the southern flank of the South Atlantic
194 and South Indian Subtropical High (4, 18). Higher sea level
195 pressure has been invoked as the cause of fewer extratropical
196 cyclones over the South Atlantic and of a southward shift of the
197 moisture corridors contributing to winter rainfall (3). Other
198 studies (4) find no significant regional trends over the last forty
199 years in the number of cold fronts making landfall over SSA,
200 but highlight the shorter duration of rainfall events associated
201 with cold fronts due to larger sea level pressure during post-
202 frontal days. Positive significant trends in sea level pressure
203 have been observed in the Southern Hemisphere over the last
204 forty years and have been related to the multidecadal expansion
205 of the Southern Hemisphere's summer and fall Hadley Cell
206 (15, 16, 18). In SPEAR_MED, the forced (i.e., ensemble mean)
207 decadal changes in sea level pressure are visible in the period
208 1980-2020 (SI Appendix, Fig. S9), with the typical patterns
209 that might dominate at end of the twenty-first century (SI
210 Appendix, Fig. S10) emerging around 2000-2010. This is in
211 agreement with previous studies (16, 17) suggesting that the
212 forced signal associated with the expansion of the Hadley
213 Cell has emerged above the noise of internal variability in the
214 Southern Hemisphere in the 2000-2010 decade.

215 There is an evident seasonality in the projected large scale
216 circulation anomalies over the South Atlantic Ocean and south
217 of SSA, with the most evident forced signals in April-May and
218 August-September (Fig. 5). Positive anomalies of mean sea
219 level pressure are overall suggestive of a poleward shift of the
220 Hadley cell. Projected changes in the 300 hPa eddy kinetic
221 energy (a proxy for the storm track) show a southward shift of
222 the midlatitude storm track in AM and AS, but not JJ. Indeed,
223 the weakest forced signals are projected in SPEAR_MED at
224 the peak of the rainy season in June-July (Fig. 5), consistent
225 with the decadal forced mean sea level pressure signals in the
226 2010-20 decade (SI Appendix, Fig. S9) and with the percent
227 WRI reductions (SI Appendix, Fig. S8b). Remarkably, the
228 2015-2017 meteorological drought was also driven mainly by
229 April-May and August-September rainfall deficits, associated
230 with large scale anomalies more evident in, e.g., April-May, and
231 similar to those just described above (3, 4, 6). These seasonal
232 aspects of the Southern Hemisphere forced circulation changes
233 coherently suggest that future meteorological droughts might
234 indeed have a similar seasonal evolution as that in 2015-2017.

235 Comparison with other large ensembles

236 We analyzed additional large ensembles from coupled models
237 with the same or coarser resolution that can provide an impor-
238 tant context to our results and inform us about uncertainties
239 due to model differences (32, 39): SPEAR_LO, the Forecast-
240 Oriented Low Ocean Resolution model with flux-adjustment
241 (FLOR_FA), the Community EARTH System Model Large
242 Ensemble, CESM-LENS (30), and the Max Planck Institute
243 Grand Ensemble, MPI-GE (26) (see Methods and SI Appendix
244 for the evaluation of these models).

245 All models suggest a substantial rainfall reduction (SI Ap-
246 pendix, Figs. S8b, S11, S12), with CESM-LENS and MPI-GE
247 projecting a percent precipitation reduction pretty uniform
248 throughout AMJJAS. Mean sea level pressure changes are
249 overall suggestive of a poleward expansion of the descending
250 branch of the Hadley Cell (SI Appendix, Fig. S10), but with
251 anomaly patterns that are more consistent across models in
252 April-May and less consistent in June-September. Indeed, the
253 Subtropical Anticyclone response in the Southern Hemisphere
254 features larger intermodel uncertainty in the austral winter
255 (40). A more prolonged dry season into the late austral fall
256 (AM) over SSA is therefore a robust indication in terms of
257 future precipitation reduction and droughts risk.

258 Relative to SPEAR_MED, the risk estimate is lower in
259 SPEAR_LO (Fig. 2g), while FLOR suggests similar values.
260 MPI-GE, FLOR_FA and CEMS-LENS have a risk ratio larger
261 than SPEAR_MED by a factor 1.5, 1.8 and 2.8, respectively.
262 By the end of this century, all models agree on a probability
263 of occurrence for the event_1517 at least ninety times larger
264 than in the twentieth century (Fig. 2h) under the highest
265 emission scenarios (SSP5-8.5 or RCP8.5). Middle-of-the-road
266 scenarios (SSP2-4.5 or RCP4.5) tend to suggest a risk ratio
267 of about thirty, while the low-emission RCP2.6 scenario (only
268 available for MPI-GE), aiming to limit the increase of global
269 mean temperature to 2K, project a risk ratio of about 13.

270 Conclusions

271 The use of a new high-resolution large ensemble provides a
272 significantly improved ability to simulate regional-scale SSA
273 droughts in both present and future conditions despite large
274 internal climate variability. We find that the rainfall deficit
275 that led to the Day Zero drought was 5.5 times more likely due
276 to anthropogenic climate change, with a confidence interval of
277 [4,8]. We therefore are able, through the use of a model with
278 higher resolution and better climatology, to further constrain
279 the risk ratio of SSA drought at and above the original [1.4,6.4]
280 estimate from ref. (5). This highlights the usefulness of high
281 resolution climate models to study future drought risk and
282 provides additional guidance to design water management to
283 avoid extreme drought.

284 Looking at the future, our results point to a dramatic
285 increase in the risk of meteorological droughts of similar or even
286 more serious magnitude by the end of the twenty-first century.
287 Similarly to what occurred in 2015-2017, this increased risk of
288 meteorological droughts is associated with a substantial rainfall
289 reduction, especially in the shoulder season (April-May and
290 August-September).

291 A high-emission and intermediate-emission future scenario
292 are analyzed, highlighting that while there is uncertainty in
293 the increase in drought risk due to future uncertainty in forc-
294 ings, both scenarios lead to substantial increases, such that a

drought becomes a common occurrence. Combined with the likelihood of increased water demand due to a growing population (3) and increased evaporation due to higher temperatures (41), the more frequent occurrence of wintertime droughts will likely present a major challenge for managing water resources in the region without adaptation and preparation. While these results are for SSA, such shifts in drought risk are likely to occur in other arid locations with variable precipitation and large scale circulation shifts increasing the likelihood of multi-year extreme droughts. These methods could then be applied elsewhere to identify emerging drought risks.

Materials and Methods

SPEAR model and experiments. The main conclusions of this study are obtained from the Seamless System for Prediction and Earth System Research (SPEAR) (33). SPEAR represents the newest modeling system for seasonal to multidecadal prediction which incorporates new model development components that have occurred in the last decade at NOAA Geophysical Fluid Dynamics Laboratory. These include: a new dynamical core (42), revised atmospheric physics (43), a new sea ice and ocean model (44) and an enhanced land model (45). The SPEAR atmospheric model uses 33 levels in the vertical and is run at different atmospheric-land horizontal resolutions: 0.5° (SPEAR_MED) and 1° (SPEAR_LO) in this paper. The intermediate 0.5° configuration, SPEAR_MED, is a compromise between the possibility to run a large ensemble of simulations with available computation resources and retaining enough horizontal resolution to study regional climate and extremes. It is worth noting that the SPEAR_MED large ensemble features a horizontal grid-spacing (0.5°) that is finer than those used in most of the previously used large ensembles (with the exception of FLOR, (31)), thus making these GFDL ensembles a unique and unprecedented tool to study extremes and regional climate.

We use four different numerical experiments: (1) a long-term control simulation (CTRL) to evaluate unforced natural variability; (2) an ensemble driven by natural forcing only (NATURAL) to provide a baseline with only natural forcing (i.e., volcanic eruptions and solar cycles); (3) an ensemble driven by observed natural and anthropogenic forcing up to 2014 (HIST) and then according to the intermediate ($\approx +3$ K of global warming by the end of the twenty-first century) Shared Socioeconomic Pathway (SSP2-4.5) developed for the Coupled Model Intercomparison Project Phase 6 (CMIP6) (35, 46); and (4) an ensemble driven by observed natural and anthropogenic forcing up to 2014 (HIST) and then according to the CMIP6 high-emission, fossil fuel dominated ($\approx +5$ K of global warming by the end of the twenty-first century) Shared Socioeconomic Pathway (SSP5-8.5).

The 3000-year CTRL simulation is driven by CO_2 forcing kept constant at 1850 levels. Climate drifts associated with this long-term integrations are estimated to be very small and statistically insignificant for the winter SA rainfall. The 30

members of the NATURAL ensemble are driven by the same observed natural forcing (i.e., solar and volcanic) until year 2014, and by only solar forcing (quasi-11-year cycle) after 2014, with the anthropogenic forcing held fixed at the 1921 level. In the HIST+SSP5-8.5 (HIST+SSP2-4.5) ensemble, each member is driven by observed natural and anthropogenic forcing (greenhouse gases, anthropogenic aerosols, ozone) up to year 2014, and by the SSP5-8.5 (SSP2-4.5) forcing afterwards. More details about how the SPEAR large ensemble is designed can be found in Delworth et al. (2020) (33).

Model Evaluation. In addition to the model's ability to reproduce the wintertime southern African climatology (Fig. 1c-e), the performance of SPEAR_MED in simulating wintertime rainfall variability and historical trends (1951-2017) over SSA is evaluated against three different observational land rainfall datasets: the Global Precipitation Climatology Centre (GPCC) dataset (47) version 7, the Climate Research Unit high-resolution grids of monthly rainfall at the University of East Anglia (48), version 3.24, and the University of Delaware (UDEL) precipitation dataset, version 5 (<http://climate.geog.udel.edu/~climate/>), all at 0.5° resolution. The choice of these three gridded observed datasets, in place of scattered measurements from the South African Weather Service meteorological stations, is dictated by the need to be able to compare models with observations, as done in previous studies (5). The values of these three precipitation datasets for SSA are obtained from a limited number of stations and different interpolation algorithms. As a consequence, they can feature, locally, considerable differences (e.g., Fig. 1a and SI Appendix, Fig. S1). However, differences in area-averaged metrics like, e.g., the WRI, are minimal (Fig. 1b), thus making our results independent from the choice of the single precipitation dataset.

In order to have a realistic representation of the width of the distribution of rainfall anomalies, it is key that SPEAR_MED reproduces the interannual, multiannual and decadal natural variability of the SSA winter rainfall. To check this, we work out the standard deviation of the detrended full, three-year and ten-year low-pass-filtered WRI from the three observational datasets and the SPEAR_MED ensemble members over the common period 1921-2010 (SI Appendix, Fig. S3). The standard deviation of the observations is between 5 mm month^{-1} (CRU) and 6 mm month^{-1} (GPCC, UDEL) for the three-year low-pass-filtered WRI. The standard deviation values from the model range from 4 to $6.3 \text{ mm month}^{-1}$. The observed values are therefore within the range from the model, suggesting that the model has the ability to properly estimate the magnitude of three-year lasting droughts. Similarly, a good agreement between SPEAR_MED and observations exist for the standard deviations calculated from the unfiltered WRI time series (interannual variability) and from ten-year low-pass-filtered WRI (decadal and longer variability) too.

The effect of internal natural variability is large for SSA winter rainfall (27–29), thus it is not appropriate to compare observed AMJJAS rainfall trends directly with the ensemble mean or with each single ensemble member, which may show contrasting signs (SI Appendix, Fig. S2). Instead, we evaluate if SPEAR_MED's historical trends of AMJJAS rainfall are consistent with observations over SSA. To do so, we compute rainfall trends over the last 67 years (1951-2017) in GPCC,

412 CRU and UDEL, and compare them with individual members
413 of the HIST+SSP5-8.5 ensembles over the same time period.

414 If the observed trend at one grid point is within the range of
415 those simulated by the 30 HIST ensemble members, then we say
416 that the model is consistent with observations in that grid box.
417 We find that SPEAR_MED is consistent with observations
418 over most of southern Africa (SI Appendix, Fig. S13).

419 **Additional large ensembles.** To assess the robustness and
420 model-dependence of our results, we analyze five additional
421 large ensembles (see Table S1): (1) the SPEAR_LO ensemble
422 (33), (2) the GFDL Forecast-Oriented Low Ocean Resolution
423 (FLOR) model, at 0.5° land/atmosphere resolution, (3) the
424 flux-adjusted FLOR (FLOR_FA) large ensembles, obtained
425 imposing temperature and salinity flux adjustments at the
426 ocean surface to FLOR (49) (both with a land-atmospheric
427 horizontal resolution of 0.5°), (4) the Community EARTH
428 System Model Large Ensemble, CESM-LENS (30), with land-
429 atmospheric horizontal resolution of approximately 1° , and
430 (5) the Max Planck Institute Grand Ensemble, MPI-GE (26),
431 with land-atmospheric horizontal resolution of 1.8° . These ad-
432 ditional large ensembles are available with various CMIP5
433 scenarios and are documented in Table S1. An evaluation of
434 the wintertime climatology over SSA shows that these models
435 all underestimate AMJJAS mean rainfall (Fig 1c-e and SI
436 Appendix, Fig. S14 and Table S2). With the exception of
437 SPEAR_LO, these models also underestimate the standard
438 deviation of the full three-year and ten-year low-pass-filtered
439 Winter Rainfall Index (SI Appendix, Fig. S3). Critically, this
440 means they also underestimate the width of the probabil-
441 ity distribution of the three-year AMJJAS rainfall anomalies
442 (SI Appendix, Fig. S15). In particular, CESM-LENS and
443 FLOR_FA have standard deviations that are 50% and 40%
444 smaller, respectively, suggesting that they are poor tools for
445 risk analysis over SSA. As they substantially underestimate the
446 probability of occurrence of event_1517, to quantify changes
447 in risk in a manner that implicitly account for model biases we
448 use a three-year Winter Rainfall Index anomaly corresponding
449 to the 1st percentile, which is the percentile to which -11.5
450 mm/month corresponds to in observations and SPEAR_MED.

451 **Winter Rainfall Index.** In this study we focus on the regional
452 scale drought of the Western Cape. We thus use the annual
453 time series of the Winter Rainfall Index (WRI) (29) to monitor
454 interannual variability and monthly rainfall anomalies. To
455 define the WRI, we first select the grid points where at least
456 65% of the total annual rainfall occur from April to September
457 (Fig. 1c-e) and SI Appendix, Fig. S13. Then, we take the
458 areal mean of the extended winter (i.e., April-September)
459 rainfall over the irregular region defined above (Fig. 1c-e, SI
460 Appendix, Fig. S13). The WRI is thus the area-averaged
461 rainfall over the portion of SSA that experiences a dry
462 summer and a wet winter, that is a Mediterranean rainfall
463 regime. This area encompasses the region of intensely
464 irrigated agriculture surrounding the metropolitan area of
465 Cape Town as well as the water basins of the Breede and Berg
466 Rivers, where dams supplying water to Cape Town are located.
467

468 **Detectability of the mean rainfall change.** To determine where
469 and when the decadal changes in AMJJAS rainfall starts being
470 caused by external forcing and not by multidecadal variability,

471 we apply a Monte Carlo approach to the long CTRL run:
472 at each grid box, we randomly choose a 10-yr period and
473 a nonoverlapping 50-yr period (to mimic 1921-1970). Then,
474 we compute the time mean difference between the 10-yr and
475 50-yr time series. This difference is solely associated with
476 internal natural variability of the climate system. This process
477 is repeated 30 times (to mimic the 30-member ensemble), we
478 then take the ensemble mean of these differences. The whole
479 process is then repeated 10,000 times to create an empirical
480 probability distribution of these ensemble mean differences,
481 which is used to assess the detectability of decadal changes
482 in rainfall. Anomalies outside the range of the distribution
483 are attributed to external forcing and considered detectable
484 against internal climate variability (Fig. 4 and SI Appendix,
485 Figs. S11-S12).

486 **Estimation of the probability distribution.** We derive a prob-
487 ability distribution of the three-year mean WRI anomalies
488 due to natural variability alone from the long CTRL run.
489 We randomly select a 50-year and three-year sequence (non-
490 overlapping), and then calculate the anomaly of the three-year
491 period relative to the 50-year climatology. This choice mimics
492 the 2015-2017 mean minus the 1921-1970 mean. We repeat
493 this process N times (N=10,000) to form a distribution of
494 the three-year WRI anomalies (Fig. 2a-d). The probability of
495 occurrence of experiencing a three-year WRI anomaly equal
496 to or less than the 2015-2017 anomaly – as per the gridded
497 datasets – is about 1% in CTRL, and 0.7% from HIST taking
498 the average of decadal probabilities over 1921-1970, respec-
499 tively (Fig. 2e). Similarly, we estimate the distribution of
500 the four-year WRI anomaly. The probability of occurrence of
501 a WRI anomaly of the same intensity but of one additional
502 year of duration is 0.4% and 0.2% from the CTRL and HIST,
503 respectively.

504 To evaluate the decadal change in the probability of occur-
505 rence of a three-year WRI anomaly equal to or worse than
506 that of 2015-17, we empirically estimate a decadal-varying
507 probability distribution using the HIST and SSP5-8.5 (SSP2-
508 4.5) experiments. The probability distribution is estimated for
509 a 20-year time window, so that, for example, that referred to
510 2010 is built from all years from 2001 to 2020. This choice is
511 motivated by the need to have a time period not too wide in
512 order to assume the stationarity of the probability distribution,
513 but at the same time a number of instances large enough to
514 allow for sufficiently accurate estimates of probabilities of rare
515 events (e.g., 100-year return time). In a 20-year time window
516 there are eighteen different three-year WRI anomalies (relative
517 to the climatological reference period 1921-1970). This leads
518 to $18 \times 30 = 540$ different values when considering all the 30 en-
519 semble members, from which we empirically build the decadal
520 probability distribution. Once we have decadal probability
521 distribution, we can estimate the probability of occurrence, for
522 each bi-decadal period, of three-year WRI anomaly equal to
523 or less than that observed in 2015-2017 ($-11.5 \text{ mm month}^{-1}$,
524 obtained averaging GPCC, CRU and UDEL) for any random
525 three year segment within the 20-year time window. The
526 95% confidence interval in these probabilities are estimated by
527 applying bootstrap-with-replacement resampling 10,000 times.
528 The same methodology is applied to estimate the probability
529 of occurrence of four-year droughts.

530 We quantify the uncertainty in the estimate of the decadal
531 probability of occurrence, derived from only 540 different

three-year rainfall anomaly values, as follows: we take the long 3,000-year CTRL and randomly select a 50-year and three-year non-overlapping periods and estimate the difference. We repeat this step N times (with $N=10,000$) to obtain a large population sample of N three-year anomalies, from which the probability of the event $_1517$ is estimated to be $\approx 1\%$. From this large sample we then randomly draw M realizations (with replacement), with $M \leq N$ and estimate the probability of occurrence. For each value of M we repeat the last step 10,000 times and obtain 10,000 different probability estimates which allows us to estimate the 95% confidence interval (SI Appendix, Fig. S4b). As expected, the confidence interval decreases with M up to approximately [0.9%,1.2%] for $M=10,000$. For values of M less than 300, the uncertainty is so large that it is impossible to have any sensible estimate of the probability of the event. For $M=540$, the confidence interval is approximately [0.5%,1.7%], which we can consider sufficiently accurate for our purposes.

Joint probability distribution of drought intensity and duration. The probability distribution of a drought in the Cape Town's Mediterranean area as a function of duration and intensity is estimated from the historical and projected AMJJAS WRI anomaly time series. The focus in this paper is on severe droughts, therefore we select, for each time series, all contiguous years for which the WRI anomaly is below -0.75 standard deviation (≈ -6 mm month⁻¹). With this choice we exclude years that were moderately and very moderately dry. For each of these segments, we work out the mean WRI anomaly by averaging the annual WRI anomaly values over the whole segment. We choose a 2 mm month⁻¹ \times 1 year bin (Fig. 3) to work out the percentage of the droughts within each bin. The analysis is performed for the 1921-1970 time period, and for the periods 2011-2040, 2041-2070, 2071-2100. To evaluate if the probability differences relative to 1921-1970 are attributable to anthropogenic climate change, we apply the same method to the 3,000-year CTRL. We randomly select a 50-year and a 30-year non-overlapping time spans, and compute the number of droughts for each duration-drought intensity bin. We repeat this 30 times to mimic the 30-member ensemble and so work out the probability differences between the 50-year and 30-year periods. The whole process is then repeated 10,000 times to create an empirical probability distribution of the probability differences for each bin: anomalies outside the range of the distribution are attributed to external forcing and considered detectable against internal climate variability.

ACKNOWLEDGMENTS. We thank A. T. Wittenberg, H. Murakami, P. C. D. Milly and two anonymous reviewers for their comments and suggestions. This report was prepared by S. P. under award NA18OAR4320123 from the National Oceanic and Atmospheric Administration, U.S. Department of Commerce. The statements, findings, conclusions, and recommendations are those of the author(s) and do not necessarily reflect the views of the National Oceanic and Atmospheric Administration, or the U.S. Department of Commerce.

1. E Archer, W Landman, J Malherbe, M Tadross, S Pretorius, South Africa's winter rainfall region drought: A region in transition? *Clim. Risk Manag.* **25**, 100188 (2019).
2. R Parks, M McLaren, R Toun, U Rivett, Experiences and lessons in managing water from Cape Town. *Grantham Inst. Brief. Pap.* **29**, 1-18 (2019).
3. PM Sousa, RC Blamey, CJC Reason, AM Ramos, RM Trigo, The 'Day Zero' Cape Town drought and the poleward migration of moisture corridors. *Env. Res. Lett.* **13**, 124025 (2018).
4. NJ Burls, et al., The Cape Town "Day Zero" drought and Hadley cell expansion. *npj Clim. Atmospheric Sci.* **2**, 2-27 (2019).
5. FEL Otto, et al., Anthropogenic influence on the drivers of the Western Cape drought 2015-2017. *Environ. Res. Lett.* **13**, 124010 (2018).

6. P Mahlalela, RC Blamey, CJC Reason, Mechanisms behind early winter rainfall variability in the southwestern Cape, South Africa. *Clim. Dyn.* **53**, 21-39 (2019).
7. City of Cape Town, Water Outlook 2018 (Rev. 25) 20 May 2018. *Dep. Water Sanitation*, 1-16 (2018).
8. G Simpkins, Running dry. *Nat. Clim. Chang.* **8**, 369-369 (2018).
9. P Woiski, How severe is Cape Town's "Day Zero" drought? *Significance* **15**, 24-27 (2018).
10. M Muller, Cape Town's drought: don't blame climate change. *Nature* **559**, 174-176 (2018).
11. Z Bischoff-Mattson, et al., Shape of a water crisis: practitioner perspectives on urban water scarcity and 'Day Zero' in South Africa. *Water Policy* **22**, 193-210 (2020).
12. J Huang, et al., Dryland climate change: Recent progress and challenges. *Rev. Geophys.* **55**, 719 - 778 (2017).
13. F Lehner, et al., Projected drought risk in 1.5° C and 2° C warmer climates. *Geophys. Res. Lett.* **44**, 7419-7428 (2017).
14. BI Cook, JE Smerdon, R Seager, S Coats, Global warming and 21st century drying. *Clim. Dyn.* **43**, 2607-2627 (2014).
15. J Lu, GA Vecchi, T Reichler, Expansion of the Hadley cell under global warming. *Geophys. Res. Lett.* **34**, L06805 (2007).
16. DJ Amaya, N Siler, SP Xie, AJ Miller, The interplay of internal and forced modes of Hadley Cell expansion: lessons from the global warming hiatus. *Clim Dyn* **51**, 305-319 (2018).
17. PW Staten, J Lu, KM Grise, SM Davis, T Birner, Re-examining tropical expansion. *Nat. Clim. Chang.* **8**, 768-775 (2018).
18. K Grise, et al., Recent Tropical Expansion: Natural Variability or Forced Response? *J. Clim.* **32**, 1551-1571 (2019).
19. PE Curtis, P Ceppi, G Zappa, Role of the Mean State for the Southern Hemispheric Jet Stream Response to CO₂ Forcing in CMIP6 models. *Environ. Res. Lett.* **15**, 064011 (2020).
20. GA Meehl, et al., THE WCRP CMIP3 Multimodel Dataset: A New Era in Climate Change Research. *Bull. Amer. Meteor. Soc.* **88**, 1383-1394 (2007).
21. KE Taylor, SR J., GA Meehl, An overview of CMIP5 and the experiment design. *Bull. Amer. Meteor. Soc.* **93**, 485-498 (2012).
22. J Kidston, EP Gerber, Intermodel variability of the poleward shift of the austral jet stream in the CMIP3 integrations linked to biases in 20th century climatology. *Geophys. Res. Lett.* **37**, L09708 (2010).
23. P Ceppi, YT Hwang, DMW Frierson, DL Hartmann, Southern Hemisphere jet latitude biases in CMIP5 models linked to shortwave cloud forcing. *Geophys. Res. Lett.* **39**, L19708 (2015).
24. C Li, F Zwiers, X Zhang, G Li, How much information is required to well constrain local estimates of future precipitation extremes? *Earth's Futur.* **7**, 11-24 (2019).
25. K Van der Wiel, N Wanders, FM Sellen, MFP Bierkens, Added value of large ensemble simulations for assessing extreme river discharge in a 2° C warmer world. *Geophys. Res. Lett.* **46**, 2093-2102 (2019).
26. N Maher, et al., The Max Planck Institute Grand Ensemble: Enabling the Exploration of Climate System Variability. *J. Adv. Model. Earth Syst.* **11**, 2050-2069 (2019).
27. N Philippon, M Rouault, Y Richard, A Favre, The influence of ENSO on winter rainfall in South Africa. *Int. J. Clim.* **32**, 2333-2347 (2012).
28. C Reason, M Rouault, J Melice, D Jagadeesha, Interannual winter rainfall variability in SW South Africa and large scale ocean-atmosphere interactions. *Meteorol. Atmos. Phys.* **80**, 19-29 (2002).
29. B Dieppois, et al., Interannual to interdecadal variability of winter and summer southern African rainfall, and their teleconnections. *J. Geophys. Res. Atmos.* **121**, 6215-6239 (2016).
30. JE Kay, et al., The Community Earth System Model (CESM) Large Ensemble Project: A community resource for studying climate change in the presence of internal climate variability. *Bull. Amer. Meteor. Soc.* **96**, 1333-1349 (2015).
31. H Zhang, T Delworth, Detectability of Decadal Anthropogenic Hydroclimate Changes over North America. *J. Clim.* **31**, 2579-2597 (2018).
32. C Deser, et al., Insights from Earth system model initial-condition large ensembles and future prospects. *Nat. Clim. Chang.* **10**, 277-286 (2020).
33. TL Delworth, et al., SPEAR - the next generation GFDL modeling system for seasonal to multidecadal prediction and projection. *J. Adv. Model. Earth Syst.* **12**, e2019MS001895 (2020).
34. I Held, et al., Structure and Performance of GFDL's CM4.0 Climate Model. *J. Adv. Model. Earth Syst.* **11**, 3691-3727 (2020).
35. V Eyring, et al., Overview of the Coupled Model Intercomparison Project Phase 6 (CMIP6) experimental design and organization. *Geosci. Model. Dev.* **9**, 1937-1958 (2016).
36. P Milly, et al., Stationarity is dead: whither water management? *Science* **319**, 573-574 (2008).
37. Jakob, D., Nonstationarity in Extremes and Engineering Design in *Extremes in a Changing Climate: Detection, Analysis and Uncertainty*, ed. AghaKouchak A. and Easterling D. and Hsu K. and Schubert S. and Sorooshian S. (Springer, New York), pp. 363-417 (2013).
38. SD Polade, A Gershunov, DR Cayan, MD Dettinger, DW Pierce, Precipitation in a warming world: Assessing projected hydro-climate changes in California and other Mediterranean climate regions. *Sci. Rep.* **7**, 10783 (2017).
39. M Hauser, et al., Methods and model dependency of extreme event attribution: The 2015 european drought. *Earth's Futur.* **5**, 1034-1043 (2017).
40. A Fahad, NJ Burls, Z Strasberg, How will southern hemisphere subtropical anticyclones respond to global warming? Mechanisms and seasonality in CMIP5 and CMIP6 model projections. *Clim. Dyn.*, <https://doi.org/10.1007/s00382-020-05290-7> (2020).
41. P Milly, K Dunne, Potential evapotranspiration and continental drying. *Nat. Clim. Chang.* **6**, 946-949 (2016).
42. LM Harris, SJ Lin, A two-way nested global-regional dynamical core on the cubed-sphere grid. *Mon. Weather. Rev.* **141**, 283-306 (2013).
43. M Zhao, et al., The GFDL Global Atmosphere and Land Model AM4.0/LM4.0: 2. Model Description, Sensitivity Studies, and Tuning Strategies. *J. Adv. Model. Earth Syst.* **10**, 735-769 (2018).
44. A Adcroft, et al., The GFDL global ocean and sea ice model OM4.0: Model description and simulation features. *J. Adv. Model. Earth Syst.* **11** (2019).
45. P Milly, et al., An Enhanced Model of Land Water and Energy for Global Hydrologic and Earth-

- 680 System Studies. *J. Hydrometeorol.* **15**, 1739–1761 (2014).
- 681 46. BC O'Neill, et al., The roads ahead: Narratives for shared socioeconomic pathways describ-
682 ing world futures in the 21st century. *Glob. Environ. Chang.* **42**, 169–180 (2017).
- 683 47. U Schneider, et al., GPCP's new land surface precipitation climatology based on quality-
684 controlled in situ data and its role in quantifying the global water cycle. *Theor. Appl. Climatol.*
685 **115**, 15–40 (2013).
- 686 48. I Harris, P Jones, TJ Osborn, DH Lister, Updated high-resolution grids of monthly climatic
687 observations – the CRU TS3.10 Dataset. *Int. J. Clim.* **34**, 623–642 (2013).
- 688 49. G Vecchi, et al., On the Seasonal Forecasting of Regional Tropical Cyclone Activity. *J. Clim.*
689 **27**, 7994–8016 (2014).

DRAFT

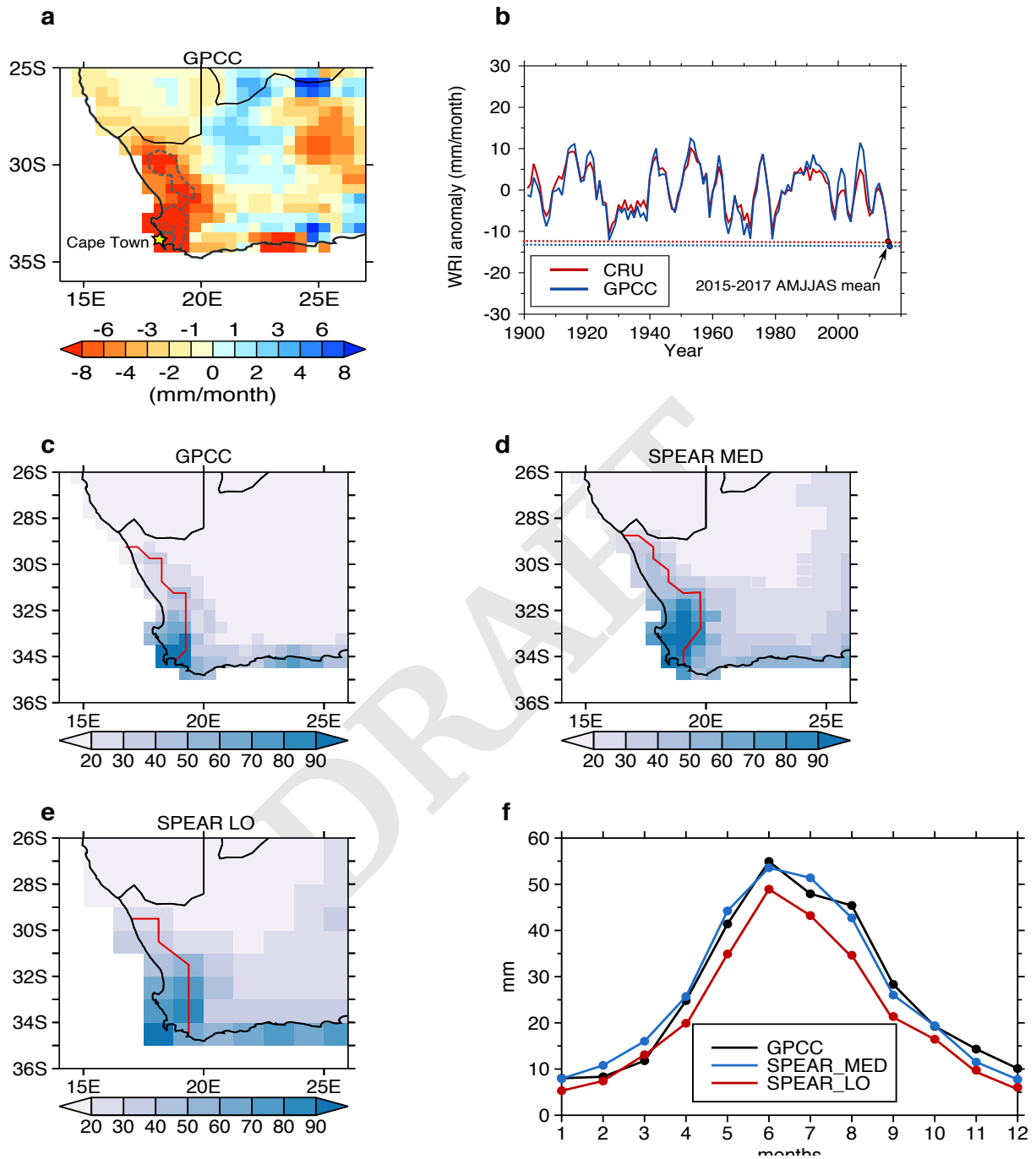


Fig. 1. a, Mean 2015-2017 AMJJAS rainfall anomaly relative to 1921-1970. The dashed (continuous) line denotes negative anomalies beyond 1 (1.5) standard deviation. **b**, Time series of the observed (GPCC, blue; CRU, red) 3-yr running mean AMJJAS Winter Rainfall Index (WRI, see Methods) from 1901 to 2017. The 2015-2017 mean is a record-breaking over the period 1901-2017. Mean 1921-1970 AMJJAS rainfall (mm/month) in **c**, observations (GPCC), **d**, SPEAR_MED, and **e**, SPEAR_LO. The red lines encircle the area receiving at least 65% of the total annual rainfall during AMJJAS used to define WRI. **f**, Monthly WRI in observations and models. Comparison of SPEAR_MED with SPEAR_LO shows how an enhanced resolution is key to capture finer scale regional details of winter rainfall in the relatively small SSA Mediterranean region.

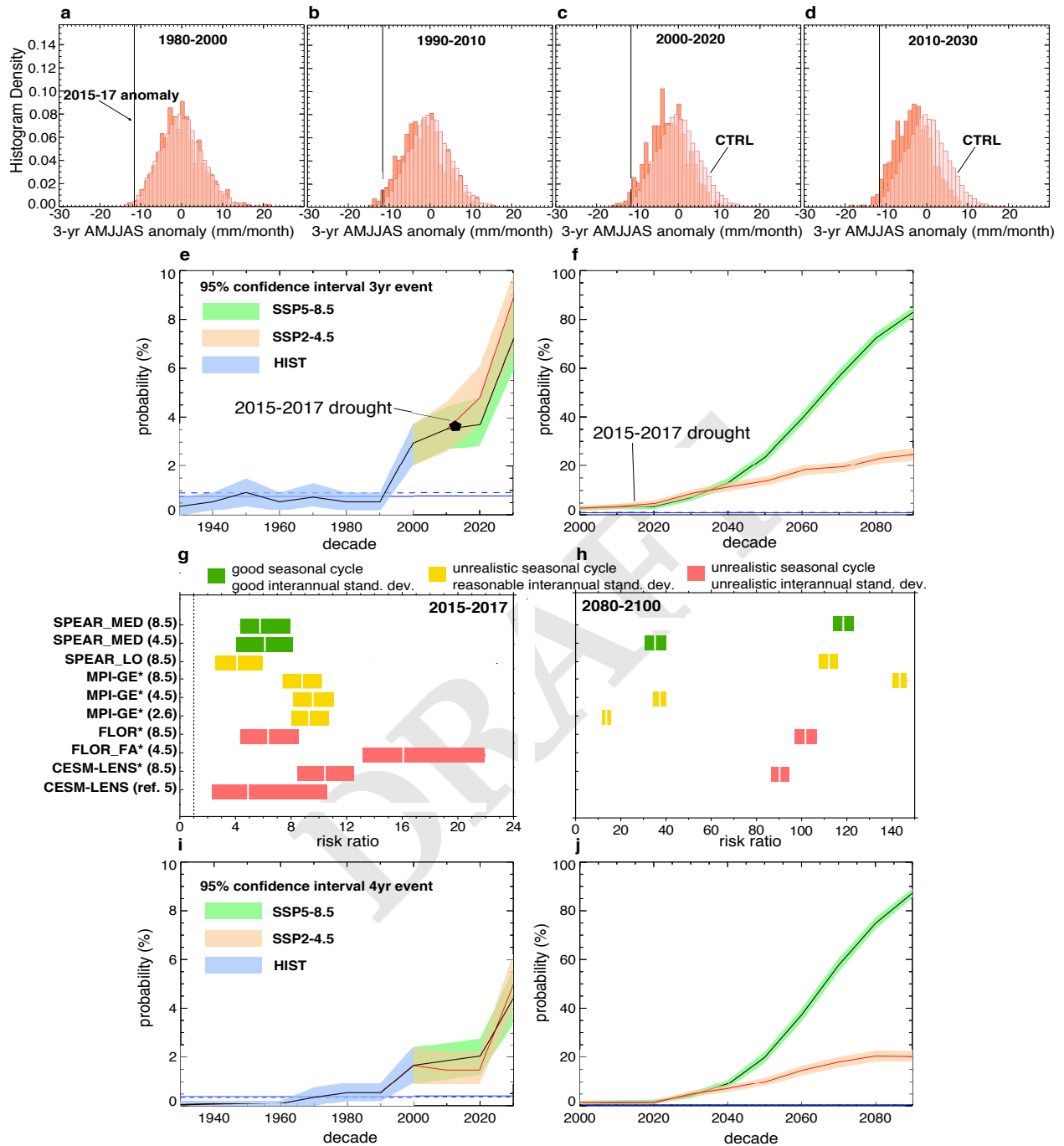


Fig. 2. a, Empirical probability distribution of the three-year winter rainfall anomalies due to internal variability alone (light pink, from CTRL) and natural variability, natural forcing and anthropogenic forcing (salmon, from SSP5-8.5) in the period 1980-2000 **b**, 1990-2010. **c**, 2000-2020. **d**, and 2010-2030. Black vertical lines represent the 2015-2017 AMJJAS rainfall anomaly (-11.5 mm/month, averaged value across GPCC, CRU, UDELAW). **e**, and **f**, Decadal probability of occurrence of a three-year winter rainfall anomaly equal to or worse than in 2015-2017 in HIST, SSP2-4.5 and SSP5-8.5. Shading denotes the 95% confidence interval from bootstrap resampling. The blue constant line denotes the CTRL probability for such an event, and the blue constant dashed line that from the NATURAL run after concatenating all 30 ensemble members. **g**, Probability (risk) ratios (to the mean 1921-1980) with 95% uncertainty intervals for event_1517 in 2015-2017, and **h**, at the end of the 21st century (2080-2100). Models are top-down ordered from the most skillful in reproducing WRI variability and seasonal cycle (SI Appendix, Fig. S5 and Table S2). Asterisk (*) denotes models for which a relative threshold (1st percentile) is used to estimate the probability (see Methods). **i**, and **j** as in **e**, **f** but for a four-year anomaly of the magnitude of the 2015-2017 drought.

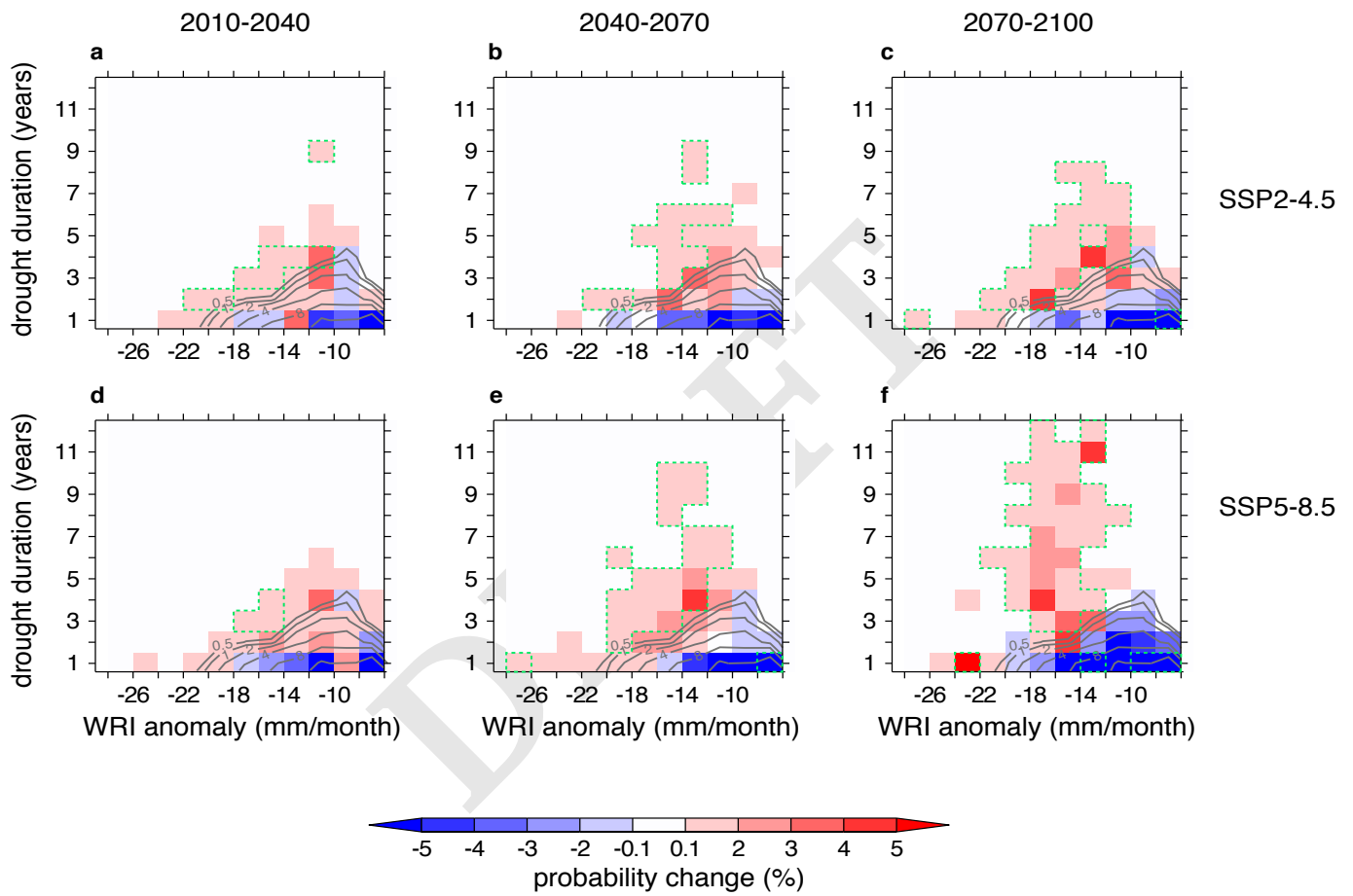


Fig. 3. Change of probability of large annual AMJJAS rainfall anomalies ($\leq -0.5\sigma$) as a function of duration (years) and intensity (mean WRI anomaly over the drought duration period) for the, **a**, 2010-2040 period relative to 1921-1970 baseline (contours), **b**, 2040-2070 period, and, **c**, 2070-2100 period under SSP2-4.5. Green dashed line encircles values that are outside the range of natural variability. **d-f** As in **a-c** but for the SSP5-8.5 pathway.

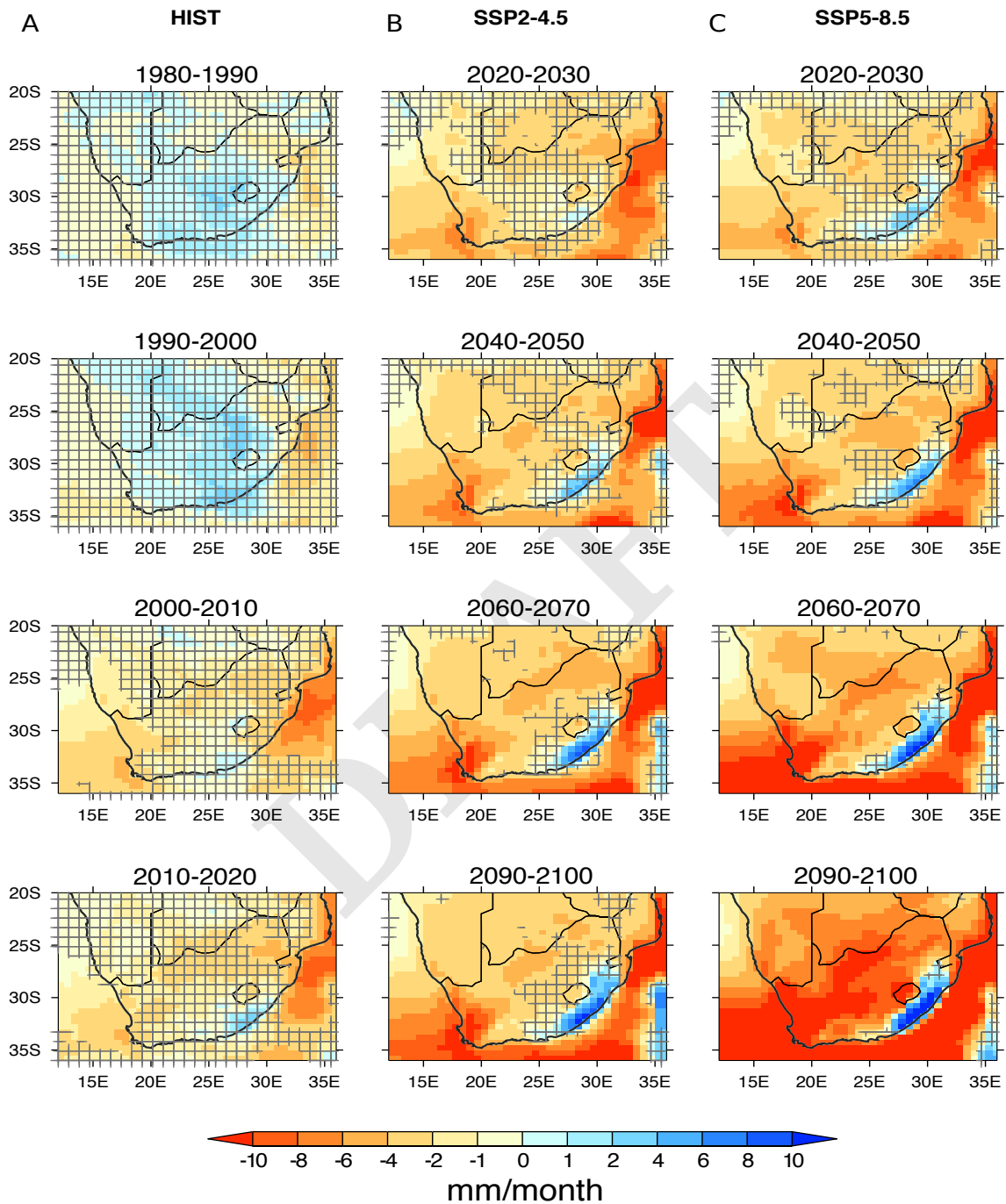


Fig. 4. Decadal evolution of wintertime (AMJJAS) rainfall mean anomalies (ensemble average, shading) relative to the 1921-1970 climate from the **a**, HIST, **b**, SSP2-4.5, and **c**, SSP5-8.5 runs. Gray crosses denote changes in wintertime rainfall mean state that are not distinguishable from internal climate variability as estimated from fully coupled control simulations (see Methods for details).

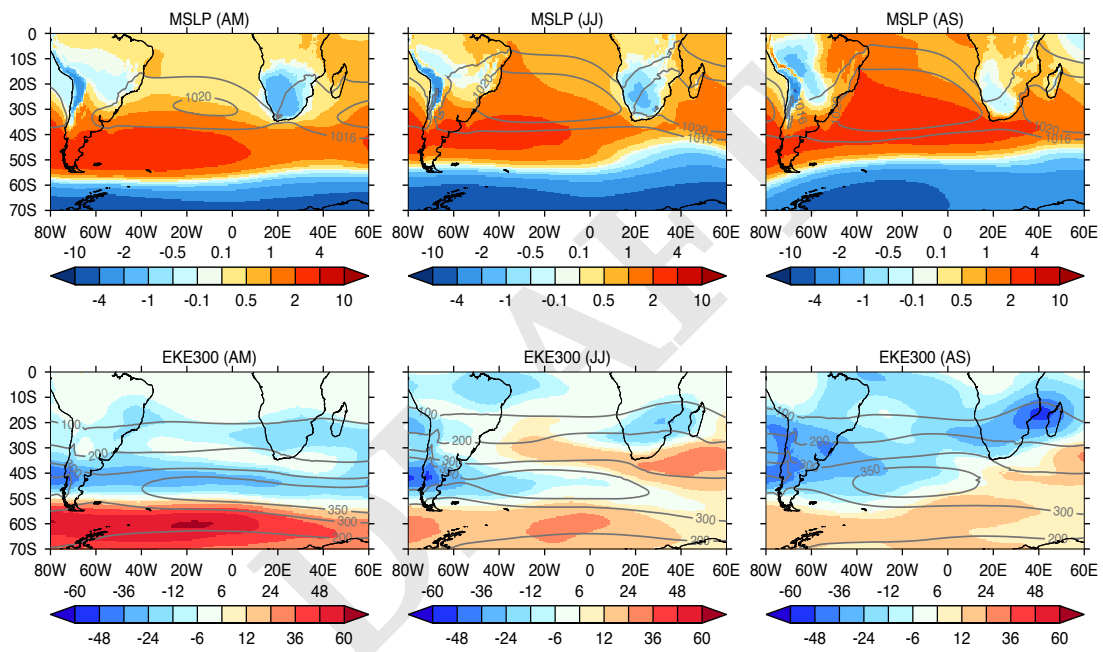


Fig. 5. Ensemble mean anomalies (shading) of April-May (AM), June-July (JJ) and August-September (AS) sea level pressure (upper row; hPa) and 300-hPa eddy kinetic energy ($\text{m}^2 \text{s}^{-2}$) for the period 2071-2100 relative to 1921-1970. Contours denote the 1921-1970 climatological values.